signal intensity as a function of time delay between the preparation and detection laser pulses.
38. The angular distribution is found by systematically translating the probe laser beam parallel to the surface at a distance of ~2 cm.
39. The average kinetic energy during the collision is ~2000 m/s, due to the strongly attractive anionic potential.

40. We are very grateful to the Air Force Office of Scientific Research, which has supported this research even in the most difficult times, and to the Santa Barbara Laser Pool, funded by the NSF, which provided equipment essential to this work. We are also grateful for the contributions of H. Hou for his development of electron transfer models and for many stimulating discussions during the early phases of this work. A.M.W thanks K. O. Sullivan, who was and continues to be extremely helpful with ab initio calculations. We all express special thanks to J. Brauman, who was a wonderful sounding board in the early stages of manuscript preparation.

6 June 2000; accepted 18 August 2000

Dynamically Controlled Protein Tunneling Paths in Photosynthetic Reaction Centers

Ilya A. Balabin and José N. Onuchic*

Marcus theory has explained how thermal nuclear motions modulate the energy gap between donor and acceptor sites in protein electron transfer reactions. Thermal motions, however, may also modulate electron tunneling between these reactions. Here we identify a new mechanism of nuclear dynamics amplification that plays a central role when interference among the dominant tunneling pathway tubes is destructive. In these cases, tunneling takes place in protein conformations far from equilibrium that minimize destructive interference. As an example, we demonstrate how this dynamical amplification mechanism affects certain reaction rates in the photosynthetic reaction center and therefore may be critical for biological function.

Electron transfer (ET) reactions play a key role in living systems, particularly in bioenergetic pathways. Most of these reactions in biological systems involve large separations (5 to 20 Å) and therefore have a very weak tunneling coupling between the donor (D) and the acceptor (A) sites. This coupling is called the electronic matrix element (T_{DA}). In this weak coupling regime, the ET rates are the product of the square of T_{DA}, as expected from perturbation theory and the probability of the donor and acceptor forming a resonant activated complex (Marcus theory) (*1*–*5*). About a decade ago, Beratan and Onuchic developed the Pathways method to estimate these T_{DA}'s and to understand the tunneling mechanism in proteins. The Pathways method assumes that tunneling occurs via a dominant pathway tube (a family of similar pathways, and that the decay through this tube can be quantified as a product of contributions from covalent bonds, hydrogen bonds, and through-space jumps (*6*, *7*). This approach has been widely used by the experimental community (*2*, *3*, *8*). However, the Pathways method has two major limitations: It does not include the possibility of interference among multiple paths, and the paths are determined with the "frozen" (crystallographic) protein structure, without accounting for protein motions.

In this report, we go beyond the Pathways method. Our results show that for ET reactions dominated by a single pathway tube (or a few tubes that interfere constructively), corrections due to protein dynamics are minor. The situation reverses when the assumption of a single pathway tube breaks down, and ET involves multiple tubes with destructive interference. T_{DA}'s are now sensitive to conformational details and nuclear dynamics. Calculations with a single frozen conformation provide an incorrect answer: Tunneling is controlled by far-from-equilibrium protein conformations, where one or few tubes dominate, thereby minimizing destructive interference.

To demonstrate this concept, the dynamical effects on T_{DA} in a bacterial photosynthetic reaction center (BPRC) are explored. The BPRC is a large transmembrane protein-cofactor complex that mediates electron and proton transfer reactions that convert light into chemical energy (*9*–*16*). We investigate the ET reactions from the pheophytin (B_{ph}) to the primary quinone (Q_A) and from the latter to the secondary quinone (Q_B), with a focus on the effects of local nuclear dynamics. Although dynamical effects on T_{DA} have been observed in previous calculations (*17*–*19*), no consistent theoretical approach has been developed yet. We provide a quantitative description of this new mechanism of dynamic control, which we name dynamical amplification. We also discuss another dynamical control mechanism, conformational gating, which was recently suggested from a high-resolution x-ray analysis of BPRC (*9*). That analysis revealed that the transition from the dark structure (Q_B in its neutral form) to the light structure (negatively charged Q_B) consists mostly of flipping and moving of the Q_B ring in its binding pocket (*10*). We show that both dynamical amplification and conformational gating are critical in providing efficient electron transfer between the quinones.

For both the dark and the light BPRC structure, T_{DA} calculations were performed with the Green's function technique (to quantify the electron tunneling propagation through the protein) with a standard extended Huckel electronic Hamiltonian in a bonding and antibonding orbital basis (*5*, *20*, *21*). The calculations included B_{ph}, Q_A, Q_B, the iron ion, and the relevant protein environment (Trp^{L100}, Met^{M256}, Trp^{M252}, Met^{M218}, His^{M219}, His^{L190}, His^{L230}, Glu^{M234}, and His^{M266}; the superscript indicates the BPRC chain and the amino acid position in that chain). To compute the average square effective coupling $\langle T_{DA}^2 \rangle$, the Green's functions were evaluated for several conformations ("snapshots"), which were obtained by using molecular dynamics (MD). In addition, T_{DA} was computed for the crystallographic and the "average" conformations (nuclear coordinates averaged over the MD runs).

The MD simulations were performed for both the dark and the light structures with the consistent valence force field (*22*) for the BPRC fragment and for all amino acids within 8 Å from it. In this initial analysis, we are mainly interested in demonstrating how competition among different tubes leads to dynamical amplification, and we therefore limited dynamics to small nuclear motions by imposing a set of restraints (*23*). All backbone atoms were fixed, and all other heavy atoms were pulled to their positions in the crystallographic structure by harmonic restraining forces. By choosing the restraining force constant, we controlled the root mean square deviation (rmsd) of these heavy atoms. The rmsd between the crystallographic and the average conformations was about 0.35 Å, and the rmsd between any snapshot and the average conformation was about 0.25 Å. The structures were first equilibrated for 3 ps, followed by a 15-ps MD run with a 0.5-fs time step. A snapshot conformation was saved every 50 ps, leading to a set of 301 snapshots for each MD run.

To quantitatively describe the degree to which nuclear dynamics affect the effective coupling, we introduced the coherence parameter $C = \langle T_{DA} \rangle^2 / \langle T_{DA}^2 \rangle$. Given that $\langle T_{DA}^2 \rangle = \langle T_{DA} \rangle^2 + \langle \delta T_{DA}^2 \rangle$, where $\langle \delta T_{DA}^2 \rangle$ is the mean square deviation, C falls in the range between zero and one. In the limit where the dynamic variations of the Green's function

Department of Physics, University of California at San Diego, La Jolla, CA 92093–0319, USA.

*To whom correspondence should be addressed. E-mail: jonuchic@ucsd.edu

are small, C approaches 1, whereas when the dynamical changes are large in comparison with the average values, C is close to zero.

To identify the structural groups most relevant for mediating the dominant pathway tubes, the tunneling coupling was calculated for the BPRC fragment ($T_{DA}^{(0)}$) and a number of modifications in which one amino acid was removed ($T_{DA}^{(i)}$ for the ith amino acid removed). The relevance of the ith amino acid was quantitatively described by the ratio (*24*, *25*) ($\log|T_{DA}^{(i)}/T_{DA}^{(0)}|^2$). The importance of individual orbital interactions that mediate through-space jumps was characterized in a similar way.

Between B_{ph} and Q_A, the dominant pathway tubes for the dark and the light BPRC structures are similar. Most of the effective coupling (about 80%) is mediated by tubes through the Trp^{M252} (*26*), and the interference regime is primarily defined by the through-space jumps from B_{ph} to the tryptophan and from the latter to Q_A. The first step is mediated by two through-space interactions between the B_{ph} and tryptophan σ orbitals, which form two parallel tubes of comparable strength and the same phase, leading to constructive interference (Fig. 1). At the second step, a strong interaction between the π orbitals on the tryptophan and the Q_A [similar to the p-σ bonds as in DNA ET (*27*)] connects the two pathway tubes into a single dominant one. A weaker alternative pathway (about 20% of T_{DA}^2 mediated by Met^{M218} and His^{M219} has a minor effect. The interference is predominantly constructive, and T_{DA}, and therefore the reaction rate (k_{ET}), are weakly sensitive to the protein environment, except for Trp^{M252}.

Between Q_A and Q_B, the dominant pathway tubes are similar for the dark and the light BPRC structures, except around Q_B. In the dark structure, Q_B is in the distal conformation, which is farther from the iron ion by about 4.3 Å than in the light structure (proximal conformation) (*9*). The transition from the dark to the light conformation (flipping and moving of Q_B) shortens the pathway by five covalent steps and replaces a through-space jump by a hydrogen bond, increasing k_{ET} by about three orders of magnitude (Fig. 2). This conformational gating, suggested in (*10*), is critical for efficient coupling. We, however, focus on an additional mechanism that involves local nuclear dynamics rather than global motion of Q_B. We explore how these dynamics affect the interference among the dominant pathways.

For the transfer from Q_A to Q_B, the interference regime is defined by the multiple pathway tubes between the quinones, which go through their neighbor histidines, and the coordination environment of the iron ion (Fig. 2). The tubes are mediated between Q_A and His^{M219} by a hydrogen bond and a few strong through-space interactions, which have similar strengths but different phases, leading to destructive interference. Between His^{L190} and Q_B, the tubes are mediated by similar interactions, which also contribute to the destructive interference. In addition, the metal bonds with His^{L230}, Glu^{M234}, and His^{M266} form a complex network interconnecting the pathway tubes. Altogether, these features result in a pronounced competition between constructive and destructive interference among the multiple tubes, as indicated by the high sensitivity of the effective coupling to small structural changes.

These different interference regimes lead to different control mechanisms for the two ET reactions, as shown in Figs. 1 and 2, respectively. Because the contributions from the dominant pathway tubes between B_{ph} and Q_A are in phase, the effective coupling is almost insensitive to structural details and dynamical modulation of the dominant pathway strengths. As shown in Fig. 1, the square of T_{DA} (and therefore k_{ET}) for the crystallographic and average conformations and $\langle T_{DA}^2 \rangle$ are very similar for both the dark and light structures, indicating the the ET rate is weakly sensitive to the choice of conformation. Consistently, the coherence parameter C is close to 1, indicating that the dynamical effects are minor. Tunneling is controlled by the overall bridge structure and not by structural details or nuclear dynamics.

In contrast, competition between destructive and constructive interference dominates the ET mechanism between Q_A and Q_B. T_{DA} (and therefore k_{ET}) are sensitive to the choice of protein conformation, as observed by the substantial difference between the k_{ET}'s for the crystallographic and the average conformations. This ET rate is also strongly modulated by the nuclear dynamics, as indicated by C close to zero (Fig. 2). This dynamical amplification makes $\langle T_{DA}^2 \rangle$ almost three orders of magnitude larger than T_{DA}^2 for the crystallographic conformation for both the light and dark structures (Fig. 2). Therefore, T_{DA} calculations need to include the "nonequilibrium" conformations; calculations based on a single conformation may be grossly misleading. This ET mecha-

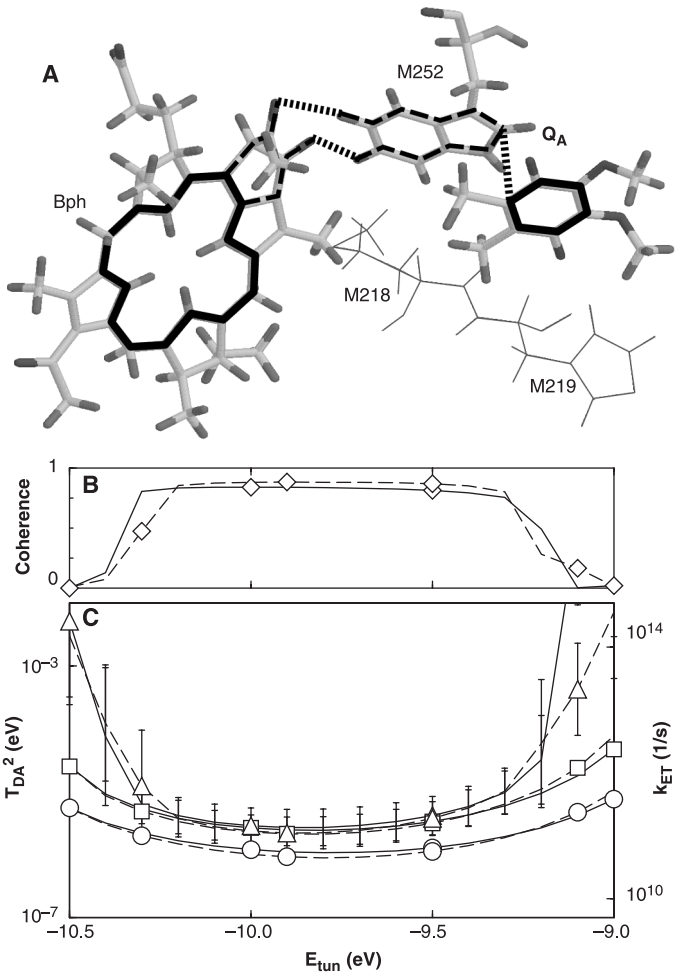

Fig. 1. The dominant pathway tubes and the effective coupling between B_{ph} and Q_A are similar for the dark [dashed lines in (B) and (C)] and the light [solid lines in (B) and (C)] structures. (**A**) Diagram that includes the donor and acceptor sites and the relevant tunneling mediating residues. The donor and the acceptor are marked by solid lines, the covalent part of the pathway tubes is shown in dashed lines, and the through-space interactions are indicated by dotted lines. The two similar dominant tubes (mediated by a through-space interaction) between the B_{ph} and the Trp^{M252} that connect into a single tube between Trp^{M252} and Q_A are highlighted. The energy range shown in (B) and (C) represents the biologically relevant tunneling energies in the middle of the main gap between σ and π – π* states. Typical tunneling energies are in the middle of this range. E_{tun} represents the energy of the electron that tunnels between the donor and the acceptor. (**B**) At the relevant energies, the coherence parameter $C = \langle \tilde{G} \rangle^2 / \langle \tilde{G}^2 \rangle$ is close to 1, indicating that dynamical effects on the coupling are minor. (**C**) The square effective couplings (left vertical axis) and the maximum ET rate k_{ET} (right vertical axis) for the crystallographic conformations (circles) and the average conformations (squares) and the dynamically averaged square effective coupling ($\langle T_{DA}^2 \rangle$, triangles) are all similar for both the dark and the light BPRC structures.

nism can be illustrated by artificially removing part of the destructive interference in the calculations by selectively pruning some interactions between the iron and the histidines and between the quinones and the histidines. An increase in C is observed, but it is still too small to justify one (or a few) dominant tube. Although this pruning removes some destructive interference, it also reduces constructive interference, making this analysis very qualitative. Finally, both this dynamical amplification and conformational gating, moving Q_B from the dark to the light position, are needed to account for the experimentally observed k_{ET}.

The results above made it possible to investigate the validity of the Pathways-like models. To compare our results with Pathways calculations and experiments, we converted the T_{DA}'s to the maximum rate using an optimized (activationless) ET reaction with a reorganization energy about 0.1 eV, which provided $k_{ET} \approx 5 \times 10^{16} \langle T_{DA}^2 \rangle$ s^{-1} (T_{DA} is in electron volts) (*5*). At the Pathways level, T_{DA} is proportional to a product of all decays in the dominant pathway tube (*5*, *6*). This approach is in agreement with previous Pathways-level calculations (*7*, *28*) and other methods (*29*, *30*), providing a maximum rate of about 10^{13} s^{-1} at distances of about 3 Å.

Between B_{ph} and Q_A, our calculations provide a maximum rate k_{ET} of 10^{11} s^{-1}, which is similar to the experimental value of 10^{10} s^{-1} (*10*). k_{ET} computed with the conventional Pathways method is slightly slower, because the correct dominant tube is partially composed by p-σ bonds, similar to ET in DNA (*27*). Still, the Pathways picture holds. Between Q_A and Q_B, the situation is reversed because several tubes constructively and destructively interfere among them. For the light structure, our calculations for the crystallographic conformation provide a maximum k_{ET} of about 10^3 s^{-1}, which is substantially smaller than observed in experiments. For the average structure, k_{ET} of about 10^1 s^{-1} is even slower. Therefore, the dynamical amplification is needed increase k_{ET} to about 10^6 s^{-1}, which still is slow compared to the Pathways value of 10^{10} s^{-1}, because destructive interference cannot be fully eliminated. Our computed rate is slightly faster than the experimental result of 10^4 s^{-1}, which is expected because our calculation does not include corrections for conformational gating (*10*). In addition to these corrections, direct comparison to experiments should be done with caution because we have not incorporated fully realistic dynamics. This may increase dynamical amplification even further, consistent with T_{DA} predicted by recent experiments (*11*).

How dynamics affect electron tunneling in proteins has been a central question for the biological electron transfer community. When tunneling is dominated by a single or a few pathway tubes, dynamical effects are small and calculations performed with a "frozen" protein give reasonable results. Dynamical amplification, however, becomes important when T_{DA} is mediated by multiple pathway tubes that are destructively interfering. In this case, tunneling is dominated by protein configurations that are far from equilibrium, where the destructive interference is substantially reduced. The competition between the occupation probability of these configurations and their ability to reduce destructive interference determines the tunneling mechanism.

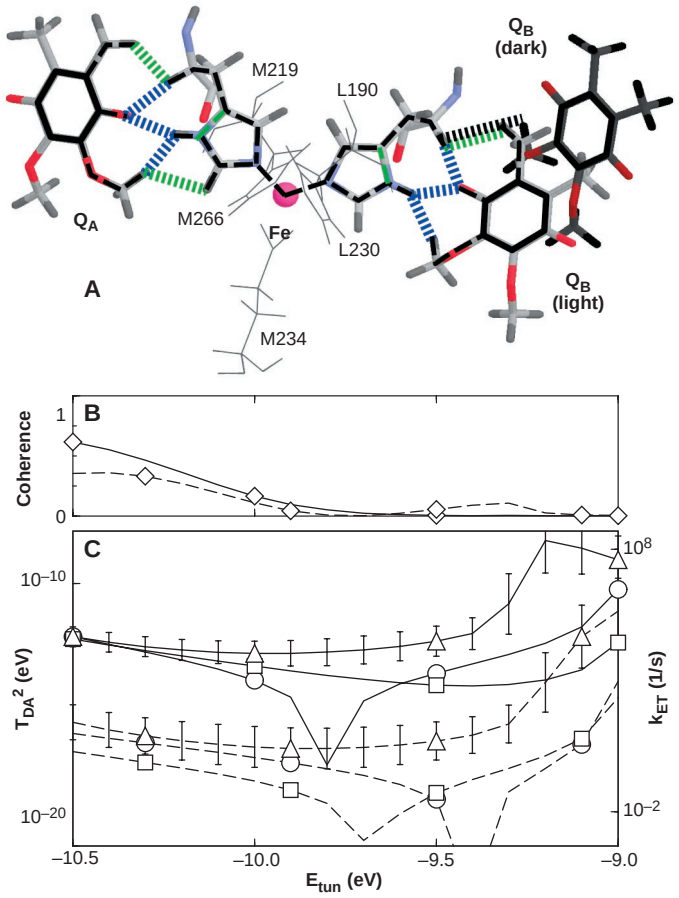

Fig. 2. (**A**) Diagram of the donor and acceptor sites and the relevant tunneling mediating residues. The secondary quinone is shown in both the distal and the proximal positions, which correspond to the dark [dashed lines in (B) and (C)] and the light [solid lines in (B) and (C)] structures, respectively. The multiple pathway tubes that mediate the coupling between Q_A and Q_B include through-space interactions between the quinones and the histidines (the stronger ones are drawn in green and blue to show the different signs of their contributions to T_{DA}) and a complex network of interactions around the iron (not shown for clarity). Interactions to Q_B are displayed only for the light structure, except for the strongest one in the dark structure, which is shown in black. These large numbers of pathway tubes will be in phase or off phase with each other, leading to a competition between destructive and constructive interference for the tunneling mechanism. The energy range in (B) and (C) and the most typical tunneling energies are described in Fig. 1. (**B**) At the relevant energies, the coherence parameter C is close to zero, indicating that the coupling is dynamically controlled. (**C**) T_{DA} (and therefore k_{ET}) is sensitive to the structural details; the couplings for the crystallographic conformations (circles) and the average conformations (squares) are substantially different. For both the light and the dark structures, the dynamical amplification makes $\langle T_{DA}^2 \rangle$ (triangles) larger by about three orders of magnitude at the relevant energies. For the light structure, the coupling is about three orders of magnitude larger than for the dark one (conformational gating).

References and Notes

1. R. A. Marcus and N. Sutin, *Biochim. Biophys. Acta* **811**, 265 (1992).
2. D. S. Bendall, Ed., *Protein Electron Transfer* (BIOS Scientific Publishers, Oxford, 1996).
3. I. Bertini, H. B. Gray, S. Lippard, J. Valentine, Eds., *Bioinorganic Chemistry* (University Science Books, Mill Valley, CA, 1994).
4. H. Sigel and A. Sigel, Eds., *Electron Transfer Reactions in Metalloproteins* (Dekker, New York, 1991).
5. Details of the reaction rate theory and calculations are described in supporting information available at www.sciencemag.org/feature/data/1052665.shl.
6. J. N. Betts, D. N. Beratan, J. N. Onuchic, *J. Am. Chem. Soc.* **114**, 4043 (1992).
7. J. J. Regan and J. N. Onuchic, *Adv. Chem. Phys.* **107**, part 2, 497 (1999).
8. H. B. Gray and J. R. Winkler, *Annu. Rev. Biochem.* **65**, 537 (1996).
9. M. H. B. Stowell *et al.*, *Science* **276**, 812 (1997).
10. M. S. Graige, G. Feher, M. Y. Okamura, *Proc. Natl. Acad. Sci. U.S.A.* **95**, 11679 (1998).
11. M. Y. Okamura, M. L. Paddock, M. S. Graige, G. Feher, *Biochim. Biophys. Acta Bioenerg.* **1458**, 148 (2000).
12. B. H. McMahon, J. D. Muller, C. A. Wraight, G. U. Nienhaus, *Biophys. J.* **74**, 2567 (1998).
13. A. G. Hyslop and M. J. Therien, *Inorg. Chim. Acta* **275-276**, 427 (1998).
14. W. G. Alexov and M. R. Gunner, *Biochemistry* **38**, 8253 (1999).
15. M. Bixon and J. Jortner, *J. Chem. Phys.* **107**, 5154 (1997).
16. A. M. Kuznetsov and J. Ulstrup, *Spectrochim. Acta Pt. A* **54**, 1201 (1998).
17. A. Aquino, P. Beroza, J. Reagan, J. N. Onuchic, *Chem. Phys. Lett.* **275**, 181 (1997).

18. J. Wolfgang, S. M. Risser, S. Priyadarshy, D. N. Beratan, *J. Phys. Chem.* **101**, 2986 (1997).
19. I. Daizadeh, E. S. Medvedev, A. A. Stuchebrukhov, *Proc. Natl. Acad. Sci. U.S.A.* **94**, 3703 (1997).
20. S. Priyadarshy, S. Skourtis, S. M. Risser, D. N. Beratan, *J. Chem. Phys.* **104**, 9473 (1996).
21. I. A. Balabin and J. N. Onuchic, *J. Phys. Chem.* **100**, 11573 (1996).
22. P. Dauber-Osguthorpe *et al.*, *Proteins Struct. Funct. Genet.* **4**, 31 (1988).
23. Larger nuclear motions, which we do not allow here, may even change the tube structure, leading to more pronounced dynamical effects.
24. A. Kuki and P. G. Volynes, *Science* **236**, 1647 (1987).
25. S. S. Skourtis and D. N. Beratan, *J. Phys. Chem.* **101**, 1215 (1997).
26. The mediating role of Trp^{M252} has been suggested in M. Plato, M. E. Michel-Beyerle, M. Bixon, J. Jortner, *FEBS Lett.* **249**, 70 (1989).
27. S. Priyadarshy, S. M. Risser, D. N. Beratan, *J. Biol. Inorg. Chem.* **3**, 196 (1998).
28. W. B. Curry *et al.*, *J. Bioenerg. Biomembr.* **27**, 285 (1995).
29. C. C. Page, C. C. Moser, X. Chen, P. L. Dutton, *Nature* **402**, 47 (1999).
30. I. A. Balabin and J. N. Onuchic, *J. Phys. Chem.* **102**, 7497 (1998).
31. We thank G. Feher, M. Okamura, and D. Beratan for valuable discussions. Funded by NIH (grant no. GM48043).

30 May 2000; accepted 16 August 2000

Xenon as a Complex Ligand: The Tetra Xenono Gold(II) Cation in $AuXe_4^{2+}(Sb_2F_{11}^-)_2$

Stefan Seidel and Konrad Seppelt*

The first metal-xenon compound with direct gold-xenon bonds is achieved by reduction of AuF_3 with elemental xenon. The square planar $AuXe_4^{2+}$ cation is established by a single-crystal structure determination, with a gold-xenon bond length of approximately 274 picometers. The bonding between gold and xenon is of the σ donor type, resulting in a charge of approximately 0.4 per xenon atom.

Since the creation of the first noble gas compound, $XePtF_6$, in 1962 (*1*), xenon compounds with direct bonds to fluorine, oxygen, nitrogen, carbon, xenon itself, and most recently, chlorine, have been established, with the list for krypton-bonded elements being much shorter. All these bonded atoms are electronegative main-group elements. Noble gas chemistry would be greatly enhanced if xenon (or other noble gases) could be bonded directly to metal atoms or ions.

There have been indications that metal-xenon bonds can be formed. In noble gas matrices, the complexes $(CO)_5Mo \ldots Xe$, $(CO)_5W \ldots Kr$, $(CO)_5Mo \ldots Kr$, and $(CO)_5Fe^+ \ldots Kr$ (*2*) have been detected. In supercritical Xe and Kr solutions, short-lived transients containing xenon or krypton metal bonds have been observed many times (*3*). The $Au\text{-}Xe^+$ ion has also been detected by mass spectroscopy, and has been calculated with a best estimate for the bond distance of 257 pm and of 30 ± 3 kcal mol^{-1} for the bond energy (*4*). Even Ar-AuCl and Kr-AuCl have been observed by microwave spectrometry (*5*). It is also possible that a similar complex between platinum fluoride(s) and xenon was an intermediate in the seminal 1962 preparation of the first xenon compound, which was formed using elemental xenon and PtF_6 (*1*). To this day, the exact nature of the product of that reaction has not been determined (*6*).

Institut für Chemie, Freie Universität Berlin, Fabeckstrasse 34-36, D-14195 Berlin, Germany.

*To whom correspondence should be addressed. E-mail: seppelt@chemie.fu-berlin.de

The original goal of this study was the preparation of the elusive gold(I) fluoride, AuF, via the reduction of AuF_3 with a weakly coordinating agent. The reaction between AuF_3 and AsF_3 in HF/SbF_5 solution afforded $F_3As\text{-}Au \ldots F \ldots SbF_5$, the first derivative of AuF (*7*). We then replaced AsF_3 with xenon as a very mild reducing and very weakly coordinating agent, in order to reach AuF. The reaction, however, stopped at the Au^{2+} state and resulted in a completely unexpected complex, the cation $AuXe_4^{2+}$, of which dark red crystals can be grown at −78°C. Removal of gaseous xenon under vacuum results in the crystallization of $Au(SbF_6)_2$, one of the few true Au^{2+} salts that are known (*8*). Addition of Xe to Au^{2+} in HF/SbF_5 gives a dark red solution at −40C°. Because the reaction between Au^{2+} and Xe is reversible, a xenon pressure of about 10 bar (1000 kPa) is necessary to stabilize $AuXe_4^{2+}$ in solution at room temperature.

A single-crystal structure determination revealed the existence of $AuXe_4^{2+}\text{-}(Sb_2F_{11}^-)_2$ (*9*). The cation forms a regular square, with Au-Xe bond lengths ranging from 272.8(1) to 275.0(1) pm. Three weak contacts between the cation and the anion complete the coordination sphere around the gold atom with Au . . . F distances of 267.1 and 315.3 pm (Fig. 1). Shortest contacts between xenon and fluorine atoms are all about 310 pm long. The structure of the anion $Sb_2F_{11}^-$ appears quite normal. The compound is stable to about −40°C. Warming above this temperature results in liquidification, loss of gaseous xenon, and a dramatic color change from dark red to light orange.

The compound $AuXe_4^{2+}(Sb_2F_{11}^-)_2$ has also been characterized by Raman spectroscopy. In addition to bonds that are typical of the $Sb_2F_{11}^-$ anion, a very strong band is observed at 129 cm^{-1}. This is assigned to the totally symmetric stretching vibration of the $AuXe_4^{2+}$, on the basis of the prediction of this band at ~100 cm^{-1} by a number of ab initio and density functional theory calculations (Table 1) (*10*).

The calculations all predict Au-Xe bond lengths a little longer than the experimental value. The mean bond energy with respect to Au^{2+} and 4 Xe is calculated to be approximately 200 kcal mol^{-1} (Table 1). This value is reasonable considering the thermal behavior of the compound $AuXe_4^{2+}(Sb_2F_{11}^-)_2$. In the complex, xenon functions as a σ donor toward Au^{2+}. This is reflected in the calculated charge distribution within the cation, where the main part of the positive charge resides on the xenon atoms. Gold is the most electronegative transition element known, in part due to the strong relativistic effect (*11*). This may explain the large charge transfer.

In principle, the bonding between xenon and

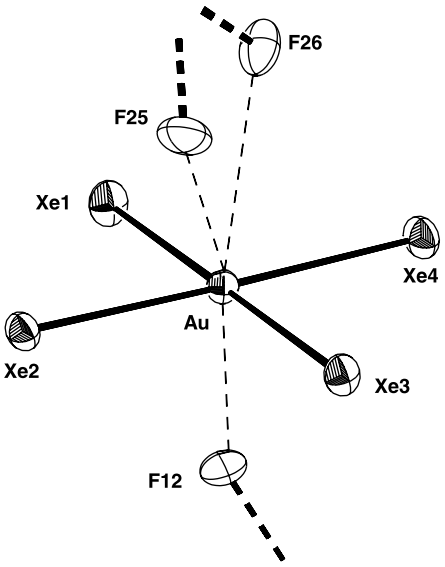

Fig. 1. Crystal structure of the cation $AuXe_4^{2+}$ in $AuXe_4^{2+}(Sb_2F_{11}^-)_2$. Atoms are represented by 50% probability ellipsoids. Shown is the cation with the three closest contacts to the anions. Distances (in pm): Au-Xe1, 273.30(6); Au-Xe2, 274.98(5); Au-Xe3, 272.79(6); Au-Xe4, 274.56(5); Au . . . F12, 267.1(4); Au . . . F26, 295.0(4); Au . . . F25, 315.3(4).